Stripped Ion–Helium Atom Collision Dynamics Within a Time-Dependent Quantum Fluid Density Functional Theory

BIJOY KR. DEY, B. M. DEB*

Theoretical Chemistry Group, Department of Chemistry, Panjab University, Chandigarh—160014, India

Received 5 March 1997; revised 7 August 1997; accepted 29 August 1997

ABSTRACT: A nonperturbative, time-dependent (TD) quantum mechanical approach is described for studying the collision dynamics between the He atom and a fully stripped ion. The method combines quantum fluid dynamics and density functional theory to solve two coupled equations: one for the trajectory of the projectile nucleus and the other for the electronic charge distribution of the target atom. The computed TD and frequency-dependent properties provide detailed features of the collision process. Inelastic and ionization cross sections are also reported. © 1998 John Wiley & Sons, Inc. Int J Quant Chem 67: 251–271, 1998

Introduction

Electronic processes occurring in collisions between two simply structured few-electron systems at low-, intermediate-, and high-projectile velocities are of great interest because such processes play an important role in fusion plasmas and astrophysics. Theoretical studies on collision dynamics mostly deal with one-electron [1–5], two-electron [6–15], and quasi-one-electron systems [16–19], while experimental works [20–23] range from one- to many-electron systems. Based on those works, the main processes (''channels'') for excitation and/or ionization during collisions between a fully stripped ion A^{q+} and a He atom can be listed as (gs means ground state, * means singly excited, ** means doubly excited):

(i) $\mathrm{He(gs)} + A^{q+} \rightarrow A^{q+} + \mathrm{He(gs)}$,

(ii) $\mathrm{He(gs)} + A^{q+} \rightarrow \mathrm{He}^* + A^{q+}$.

Correspondence to: B. M. Deb.

*Also from the Jawaharlal Nehru Centre for Advanced Scientific Research, Bangalore-560064, India.

Contract grant sponsors: Council of Scientific and Industrial Research, New Delhi, Department of Atomic Energy, Bombay; Jawaharlal Nehru Centre for Advanced Scientific Research, Bangalore.

© 1998 John Wiley & Sons, Inc.
CCC 0020-7608 / 98 / 040251-21

(All the singly excited states of He can contribute.)

(iii) $\mathrm{He(gs)} + A^{q+} \rightarrow \mathrm{He}^{**} + A^{q+}$.

(All the doubly excited states of He can contribute.)

(iv) $A^{q+} + \mathrm{He} \rightarrow A^{q+} + \mathrm{He}^{+} + e$,
(v) $A^{q+} + \mathrm{He} \rightarrow A^{q+} + \mathrm{He}^{2+} + e_1 + e_2$,
(vi) $A^{q+} + \mathrm{He} \rightarrow A^{+(q-1)} + \mathrm{He}^{+}$,

where the single electron can stay in different excited states of He^{+} and $A^{+(q-1)}$.

(vii) $A^{q+} + \mathrm{He} \rightarrow A^{+(q-1)} + \mathrm{He}^{2+} + e$,
(viii) $A^{q+} + \mathrm{He} \rightarrow (\mathrm{He}\ A^{q+})$.

Thus, a number of processes, (i)–(viii), can take place in varying proportions. Theoretically, all the atomic collisions can be divided into the following three different regions [24] depending on the relative magnitudes of the collision velocity v and the classical orbiting velocity of the active electron v_e corresponding to $\max(Z_P/n_P, \varepsilon_T)$, where Z_P is the nuclear charge of the fully stripped projectile; n_P, the quantum number of the electron when it moves into the projectile's state; and ε_T, the electronic orbital energy of the target He atom: (a) adiabatic region ($v \ll v_e$), (b) intermediate region ($v \cong v_e$), and (c) high-energy region ($v \gg v_e$). High-energy collisions can again be of two types [23]: soft collisions, characterized by small momentum transfer, and hard collisions, characterized by comparatively large momentum transfer.

There are many theoretical methods available for studying collision dynamics and all these studies aim at one/few channel(s) out of many as listed above. The high-energy region is accessible to perturbative approaches since the target electronic states are only weakly perturbed by the fast projectile and a description in terms of the target or projectile eigenstates is possible [25]. At very high velocity, excitation processes (ii) and (iii) can be accurately described by the first-order Born approximation [26] while the electron-transfer process (vii) can be dealt with by the second-order Born approximation [27]. The intermediate regions are usually tackled by coupled-channel calculations or variational procedures.

Low-energy collisions falling in the adiabatic region have been discussed infrequently. To our knowledge, most of the collision studies for two-electron systems lie in the intermediate- and high-energy regions, i.e., $E > 1$ keV. However, some noteworthy works for one-electron systems in the low-energy region exist [3–5]. In this low-energy region, although energy transfer to the electron is low, the fraction of energy transfer is higher than in high-energy collisions because the total time of the interaction is large. Thus, the electron has sufficient time during the interaction to adjust itself to the instantaneous two-center potential created by the two nuclei so that an intermediate moleculelike complex is formed [28]. The excitations (ii) and (iii) or transfers (vi) and (vii) also occur by the variation of the two-center potential with time [29]. Although a third body is required to absorb the energy released in molecule formation, a recent calculation by Macek and Wang [9] shows a significant population of the quasi Σ molecular level in a H^{+}—He collision.

Some of the theoretical methods available for studying collision dynamics from low to high velocities are (i) T-matrix calculation for a particular channel [10]; (ii) the unified atomic orbital–molecular orbital (AO–MO) matching method [6] where the time-dependent wave function (TDWF) is expanded in terms of traveling AOs; (iii) the multiple scattering method with a continuum distorted-wave approximation [7]; (iv) the MO expansion method with electron translation factors [12]; (v) differential and integrated density matrix calculation for a particular channel [30]; (vi) the AO close-coupling method [15, 31–33]; (vii) the direct solution of TD Hartree–Fock (HF) equations [11, 34, 35]; (viii) the direct solution of the time-dependent (TD) Schrödinger equation (SE) using molecular basis functions [9]; (ix) the TD quantum fluid density (QFD) functional method [13, 36]; (x) the Car–Parrinello method [37–39]; and (xi) the TD density functional method [40]. All the above studies adopt an impulse approximation, i.e., a straight-line trajectory for the projectile.

Obviously, one requires a conceptually transparent and computationally tractable formalism which can visualize the collision dynamics from ''start'' to ''finish'' by calculating the movements of both the projectile and the electron density under the combined field of two nuclei. The method should be equally applicable to high-, intermediate-, and low-energy regions; in the last case, the impulse approximation is no longer valid. The present work essentially deals with low- and intermediate-energy collisions (100 eV–10 keV).

The present article studied the collision dynamics between He and a fully stripped nucleus for

different energy and impact parameters, in terms of the trajectory of the stripped nucleus and several density-based TD quantities of the interacting system. It considers the collisional system to consist of two bodies, viz., the projectile and the electronic charge of the fixed residual target atom [41, 42]. This mixed quantum classical approach allows one to describe the projectile using classical mechanics with the feedback of electron density of the target which is treated using quantum mechanics. In treating the electronic charge of the target quantum mechanically, we adopted a method which is essentially an amalgamation of density functional theory (DFT) [43, 44] and quantum fluid dynamics (QFD) [45–47], called time-dependent quantum fluid density functional theory (TDQFDFT). Successful applications of TDQFDFT have already been made in intense-laser-atom dynamics leading to photoionization [48] and photoemission [49]; superintense-laser-atom dynamics leading to the suppression of ionization [50]; and high-energy H^+—Ne and H^+—He collisions [13, 36]. We hope that these works would lead to extensive applications of TDQFDFT to molecular dynamics, e.g., dissociation of molecules by an external field where the calculation of both nuclear and electronic motions ought to be considered.

The layout of the article is as follows: The next section describes the present approach. The third section summarizes the numerical method adopted to solve the resultant equations. The third section also lists different TD quantities required to visualize and understand the dynamical changes in electronic motion in the time-varying two-centered potential field. The fourth section discusses the results, while the fifth section makes several concluding remarks.

The Approach

The present time-dependent quantum fluid density functional method is based on a fluid dynamical interpretation of the quantum mechanical probability density and current. It regards all the electrons in the system to be distributed in 3-D space like a continuous ''classical'' fluid [13, 36, 45, 46, 48, 49] which behaves in a collective manner to any external influence. Such a consideration of electron distribution arises from a hydrodynamical ''wave function,'' $\Psi(\mathbf{r}, t)$ given by (atomic units employed throughout unless otherwise mentioned)

$$\Psi(\mathbf{r}, t) = \rho(\mathbf{r}, t)^{1/2} e^{iS(\mathbf{r}, t)}, \tag{1}$$

which directly delivers the two essential ingredients, viz., density, $\rho(\mathbf{r}, t)$ and current density, $\mathbf{J}(\mathbf{r}, t)$ required to describe a many-electron system uniquely,

$$\begin{aligned} \rho(\mathbf{r}, t) &= \Psi^*(\mathbf{r}, t)\Psi(\mathbf{r}, t) \\ \mathbf{J}(\mathbf{r}, t) &= \rho(\mathbf{r}, t)\nabla S(\mathbf{r}, t). \end{aligned} \tag{2}$$

It is shown in time-dependent DFT [51, 52] that (i) the density $\rho(\mathbf{r}, t)$ and $\rho'(\mathbf{r}, t)$ evolving from the same initial density $\rho_0(\mathbf{r}, t)$ under the influence of two potentials $V(\mathbf{r}, t)$ and $V'(\mathbf{r}, t)$ are always different provided that the potentials differ by more than a purely TD function, viz.,

$$\begin{aligned} V(\mathbf{r}, t) &\xrightarrow{\rho_0(\mathbf{r}, t)} \rho(\mathbf{r}, t) \\ V'(\mathbf{r}, t) &\xrightarrow{\rho_0(\mathbf{r}, t)} \rho'(\mathbf{r}, t) \end{aligned} \tag{3}$$

if $V'(\mathbf{r}, t) \neq V(\mathbf{r}, t) + C(t)$, then $\rho(\mathbf{r}, t) \neq \rho'(\mathbf{r}, t)$.

(ii) $$\frac{\partial}{\partial t}[\mathbf{J}(\mathbf{r}, t) - \mathbf{J}'(\mathbf{r}, t)]_{t=t_0} = -\rho_0\nabla(V(\mathbf{r}, t_0) - V'(\mathbf{r}, t_0)). \tag{4}$$

Thus, if $V(\mathbf{r}, t_0) \neq V'(\mathbf{r}, t_0)$, then $\mathbf{J}(\mathbf{r}, t) \neq \mathbf{J}'(\mathbf{r}, t)|_{t=t_0}$.

Hence, unlike stationary DFT, in TDDFT, one needs two variables ρ and $\mathbf{J}$ to characterize the many-electron system. Therefore, one must have two equations to describe the system within the density-based formalism, viz., the continuity equation

$$\frac{\partial \rho(\mathbf{r}, t)}{\partial t} + \operatorname{div} \mathbf{J}(\mathbf{r}, t) = 0 \tag{5}$$

and the force equation for the fluid consisting of constituents which interact with each other by a potential V depending on the probability density of the constituent $\rho(\mathbf{r}, t)$ at position $\mathbf{r}$:

$$\frac{d\mathbf{v}}{dt} = \mathbf{F} = -\nabla V, \text{ where } \frac{d\mathbf{v}}{dt} = \frac{\partial \mathbf{v}}{\partial t} + (\mathbf{v} \cdot \nabla)\mathbf{v}. \tag{6}$$

In view of the many-body effects among the fluid constituents, the various terms in V can be written as

$$\begin{aligned} V &= V_{KE}[\rho] + V_c[\rho] + V_{el-el}[\rho] \\ &\quad + V_x[\rho] + V_{ext}[\rho] \\ &= \frac{\delta T[\rho]}{\delta\rho} + \frac{\delta E_c[\rho]}{\delta\rho} + \frac{\delta E_{el-el}[\rho]}{\delta\rho} \\ &\quad + \frac{\delta E_x[\rho]}{\delta\rho} + \frac{\delta E_{ext}[\rho]}{\delta\rho}. \end{aligned} \tag{7}$$

In the time-dependent Thomas–Fermi (TDTF) method [53], $\delta E_x/\delta\rho = \delta E_c/\delta\rho = 0$ and $\delta T[\rho]/\delta\rho = \delta T_{TF}/\delta\rho$. Hence, the shell structure is missing in the density $\rho(\mathbf{r}, t)$ in the TDTF method. Also, the TDTF method does not resemble the TDSE. In the method developed in our laboratory (see [13, 36, 45, 46, 48, 49]), V takes the form

$$V[\rho] = \frac{\delta G[\rho]}{\delta\rho} + \frac{\delta E^c_{qu}[\rho]}{\delta\rho} + \frac{\delta E_{ext}[\rho]}{\delta\rho}, \tag{8}$$

where

$$\begin{aligned} \frac{\delta G[\rho]}{\delta\rho} &= \frac{\delta T_w[\rho]}{\delta\rho} + \frac{\delta E_x[\rho]}{\delta\rho} \\ &\quad + \frac{\delta E_c[\rho]}{\delta\rho} + \frac{\delta E_{el-el}[\rho]}{\delta\rho}, \end{aligned} \tag{9}$$

where $T_w[\rho]$, $E_x[\rho]$, and $E_c[\rho]$ are Weizsäcker kinetic energy, exchange energy, and correlation energy functionals, respectively. $E^c_{qu}[\rho]$ is a correction for the kinetic-energy functional required to obtain the correct kinetic energy for many-electron systems. $T_w[\rho]$ and $E^c_{qu}[\rho]$ jointly take care of the structure of the fluid density $\rho(\mathbf{r}, t)$. However, for one-electron systems, $\delta E^c_{qu}/\delta\rho = 0$, which is also true for two-electron HF systems. $T_w[\rho]$ is given by

$$T_w[\rho] = \frac{1}{8}\int \frac{(\nabla\rho)^2}{\rho}\, d\mathbf{r}. \tag{10}$$

The two coupled Eqs. (5) and (6) can be combined together with the help of Eqs. (1) and (8) to obtain a generalized nonlinear Schrödinger equation (GNLSE) [13] provided that $E^c_{qu}[\rho]$ does not contain any gradient term. The GNLSE is given as

$$i\frac{\partial\Psi}{\partial t} = \left[-\frac{\nabla^2}{2} + V_{eff}(\rho; \mathbf{r}, t)\right]\Psi, \tag{11}$$

where

$$V_{eff} = \frac{\delta E_x}{\delta\rho} + \frac{\delta E_c}{\delta\rho} + \frac{\delta E_{el-el}}{\delta\rho} + \frac{\delta E^c_{qu}}{\delta\rho} + \frac{\delta E_{ext}}{\delta\rho}. \tag{12}$$

This is the quantum mechanical equation for the charge density which moves in the field of the two nuclei, the fixed target (T) and the projectile (P). Below, we describe how the effect of the projectile is taken care of in the present approach.

MIXED QUANTUM-CLASSICAL (MQC) MODEL

Let the electronic charge density be described by the space coordinates $\mathbf{r} \in \mathbb{R}^3$ and the projectile described by its space coordinate $\mathbf{r}_p \in \mathbb{R}^3$. The target is kept fixed in $\mathbb{R}^3$. Let m and M be the masses of the electron and the projectile, respectively. Obviously, the interaction potential between the electrons and projectile is $V_{eff} = V_{eff}(\rho; \mathbf{r}_p, \mathbf{r})$. The basic assumption of the MQC model is that the masses differ significantly, $m \ll M$, and, therefore, the heavier particle can be modeled classically while the lighter one remains a ''quantum particle.'' In other words, the quantum particle (the electron) is described by a wave function, which, however, is a hydrodynamical ''wave function'' in the present case and obeys the GNLSE

$$i\frac{\partial\Psi}{\partial t} = \left[-\frac{1}{2m}\nabla_r + V_{eff}(\rho; \mathbf{r}, \mathbf{q})\right]\Big|_{\mathbf{q}=\mathbf{r}_p(t)}\Psi, \tag{13}$$

with a parametrized potential which depends on the location $\mathbf{r}_p(t)$ of the ''classical'' particle. The location $\mathbf{r}_p = \mathbf{r}_p(t)$ is the solution of a classical Hamiltonian equation of motion:

$$\begin{aligned} M\dot{\mathbf{r}}_p &= \mathbf{P} \\ \dot{\mathbf{P}} &= -\nabla_{r_p} U, \end{aligned} \tag{14}$$

in which the TD potential U is obtained from V_{eff} weighted with the probability of finding the quantum particle,

$$U(\rho; \mathbf{r}_p, t) = \int \rho(\mathbf{r}_p, \mathbf{r}, t) V_{eff}(\rho; \mathbf{r}_p, \mathbf{r})\, d\mathbf{r}. \tag{15}$$

Thus, the forces in Eq. (14) are the so-called Hellmann–Feynman forces [54]. Together, Eqs. (13) and (14) are the basic equations of motion of our present MQC approach.

TWO WAYS TO COMPUTE $\nabla_{r_p} U$

Case I: Let the two arguments r_p and ρ of U be independent unknowns, i.e., r_p is just a constant parameter when ρ is varied and vice versa. Then,

$$\nabla_{r_p} U = \int \rho(\mathbf{r}_p, \mathbf{r}, t) \nabla_{r_p} V_{eff}(\rho; \mathbf{r}_p, \mathbf{r})\, d\mathbf{r}. \quad (16)$$

This can be evaluated directly (see, e.g., [55, 56]).

Case II: The dependence of ρ on $\mathbf{q}$ may be taken into account, i.e.,

$$\nabla_{r_p} U = \int \rho(\mathbf{r}_p, \mathbf{r}, t) \nabla_q V_{eff}(\rho; \mathbf{q}, \mathbf{r})\, d\mathbf{r}\Big|_{\mathbf{q}=\mathbf{r}_p} + \int V_{eff}(\rho, \mathbf{q}, \mathbf{r}) \nabla_q \rho\, d\mathbf{r}\Big|_{\mathbf{q}=\mathbf{r}_p}. \quad (17)$$

This necessitates much more effort in real applications [57, 58]. In the present study, we follow case I.

The generalized nonlinear Schrödinger Eq. (11) takes the following form [48, 50] in cylindrical coordinates ($0 < \tilde{\rho} \le \infty$; $-\infty \le \tilde{z} \le \infty$; $0 \le \tilde{\phi} \le 2\pi$):

$$\left[-\frac{1}{2}\nabla^2_{\tilde{\rho},\tilde{z}} + V_{eff}(\rho; \tilde{\rho}, \tilde{z}, \tilde{\rho}_P, \tilde{z}_P, t)\right] \times \Psi(\tilde{\rho}, \tilde{z}, \tilde{\rho}_P, \tilde{z}_P, t) = i\frac{\partial}{\partial t}\Psi(\tilde{\rho}, \tilde{z}, \tilde{\rho}_P, \tilde{z}_P, t), \quad (18)$$

where

$$V_{eff}(\rho; \tilde{\rho}, \tilde{z}, \tilde{\rho}_P, \tilde{z}_P, t) = \frac{\delta E_x[\rho]}{\delta\rho} + \frac{\delta E_c[\rho]}{d\rho} + \frac{\delta E_{el-el}[\rho]}{\delta\rho} + \frac{\delta E_{T-el}[\rho]}{\delta\rho} + \frac{\delta E_{P-el}[\rho]}{\delta\rho} + \frac{\delta E^c_{qu}[\rho]}{\delta\rho}. \quad (19)$$

For the present two-electron system, $\delta E^c_{qu}[\rho]/\delta\rho = 0$. The azimuthal angle $\tilde{\phi}$ in Eq. (18) has been integrated out. Within a local density approximation, we employ the Dirac expression for the exchange energy $E_x[\rho]$ and a Wigner-type parametrized expression for the correlation energy $E_c[\rho]$ because a combination of the two is a very good approximation for $E_{xc}[\rho]$ due to partial cancellation of errors [59]. E_{el-el} is the Coulomb interaction energy between the electrons and E_{T-el} is the same between the target nucleus (He^{2+}) and the electrons. $E_P[\rho]$ is the interaction energy between the electrons and the projectile nucleus. Below, the different terms on the right-hand side of Eq. (19) are given by

$$E_x[\rho] = -\int c_x \rho^{4/3}(\mathbf{r})\, d\mathbf{r};\ \frac{\delta E_x[\rho]}{\delta\rho} = -\frac{4}{3} c_x \rho^{1/3};$$
$$c_x = \frac{3}{4\pi}(3\pi^2)^{1/3} \quad (20)$$

$$E_c[\rho] = -\int \frac{\rho}{a + b\rho^{-1/3}}\, d\mathbf{r};$$
$$\frac{\delta E_c[\rho]}{\delta\rho} = \frac{a + c\rho^{-1/3}}{(a + b\rho^{-1/3})^2}; \quad (21)$$
$$a = 9.812,\ b = 21.437,\ c = 28.582667$$

$$E_{el-el}[\rho] = \int \frac{\rho(\mathbf{r}, t)\rho(\mathbf{r}', t)}{|\mathbf{r} - \mathbf{r}'|}\, d\mathbf{r}'\, d\mathbf{r};$$
$$\frac{\delta E_{el-el}[\rho]}{\delta\rho} = \int \frac{\rho(\mathbf{r}', t)}{|\mathbf{r} - \mathbf{r}'|}\, d\mathbf{r}' \quad (22)$$

$$E_{T-el}[\rho] = -\int \frac{Z_T}{r}\rho(\mathbf{r}, t)\, d\mathbf{r};\ \frac{\delta E_{T-el}[\rho]}{\delta\rho} = -\frac{Z_T}{r} \quad (23)$$

$$E_{P-el}[\rho] = -\int \frac{Z_P \rho(\mathbf{r}, t)}{|\mathbf{r} - \mathbf{r}_P(t)|}\, d\mathbf{r};$$
$$\frac{\delta E_{P-el}[\rho]}{\delta\rho} = -\frac{Z_P}{|\mathbf{r} - \mathbf{r}_P(t)|} \quad (24)$$

$$\mathbf{r} = \hat{e}_{\tilde{\rho}}\tilde{\rho} + \dot{e}_{\tilde{z}}\tilde{z};\ r = (\tilde{\rho}^2 + \tilde{z}^2)^{1/2} \quad (25)$$

$$\mathbf{r}_P(t) = \hat{e}_{\tilde{\rho}}\tilde{\rho}_P(t) + \hat{e}_{\tilde{z}}\tilde{z}_P(t);$$
$$r_P(t) = (\tilde{\rho}_P^2(t) + \tilde{z}_P^2(t))^{1/2}, \quad (26)$$

where Z_P and Z_T are nuclear charges of the projectile and target, respectively. Relativistic contributions are not taken into account in this work because the velocity of the electron given by $v_e = v_0 + v_P$ (see Appendix A) is relatively small compared with the speed of light. In Eqs. (20)–(26), the position vector $\mathbf{r}_P(t)$ of the projectile is measured

from the origin (site of target nucleus) and $e_{\tilde{\rho}}$ and $e_{\tilde{z}}$ are the unit vectors along the radius and axis of the cylinder, respectively.

Provided that one evaluates both $\tilde{z}_P(t)$ and $\tilde{\rho}_P(t)$, which jointly determine the trajectory of the projectile, Eqs. (18)–(26) describe the complete dynamics of stripped ion–helium atom collisions in terms of the time evolution of the hydrodynamical ''wave function'' $\Psi(\mathbf{r}, t)$, which yields the TD charge density, the current density, and the pulsating two-center effective potential $V_{eff}(\rho, \mathbf{r}, \mathbf{r}_P, t)$ on which the collision process occurs. Two previous studies [13, 36] in our laboratory on collisions at high-projectile velocities assume the impulse approximation and, in one study [13], head-on collision. The present work does not make either of these two assumptions.

As mentioned before, the classical equation of motion for the projectile is given by

$$M_P \frac{d^2\mathbf{r}_P}{dt^2} = -\nabla_{r_p} U\{E_P, \rho(\mathbf{r}, \mathbf{r}_p, t); Z_T, Z_P, t\}, \quad (27)$$

where M_P is the mass of the projectile, and E_P, its kinetic energy in the laboratory coordinate system.

Numerical Solution

Equations (18) and (27) have to be solved numerically and simultaneously. The solution of Eq. (27) yields the position of the projectile in the $(\tilde{\rho}, \tilde{z})$ space at any time and follows the solution of Eq. (18) for $\rho(\mathbf{r}, t)$. The projectile is shot with a kinetic energy E_P, from a position such that it is b distance apart (impact parameter) from the target nucleus (He^{2+}) along the $\tilde{\rho}$-axis and $\tilde{z}_P^0$ distance apart along the $\tilde{z}$-axis. The incident velocity of the projectile makes an angle ϑ_0 with the axis of the cylinder. Starting from this, we perform the numerical solution by discretizing the $(\tilde{\rho}, \tilde{z})$ grid as follows:

$$\begin{aligned} \tilde{\rho}_l &= x_l^2 \\ x_l &= x_0 + (l-1)h,\ l = 1, 2, 3, \ldots, N_1 \\ \tilde{z}_m &= -\tilde{z}_0 + (m-1)h,\ m = 1, 2, 3, \ldots, N_2 \\ \tilde{z}_0 &= \left(\frac{N_2 - 1}{2}\right)h. \end{aligned} \quad (28)$$

Such a discretization effectively deals with the singularity problem arising out of the Z_T/r term in Eq. (23). The time domain is discretized as

$$t = n\,\Delta t;\ n = 1, 2, 3, \ldots, N_3. \quad (29)$$

THE SOLUTION OF EQ. (27)

In the cylindrical coordinate system, Eq. (27) can be written in a compact matrix form as follows:

$$M_P \frac{d^2}{dt^2}\begin{pmatrix} \tilde{\rho}_P \\ \tilde{z}_P \end{pmatrix} = -\begin{pmatrix} \dfrac{\partial}{\partial\tilde{\rho}_P} & \dfrac{\partial}{\partial\tilde{\rho}_P} \\ \dfrac{\partial}{\partial\tilde{z}_P} & \dfrac{\partial}{\partial\tilde{z}_P} \end{pmatrix}\begin{pmatrix} U_1 \\ U_2 \end{pmatrix}, \quad (30)$$

$$U_1 = \frac{Z_P Z_T}{\left(\tilde{z}_P^2 + \tilde{\rho}_P^2\right)^{1/2}}, \quad (31)$$

and

$$U_2 = \int V_{eff}\,\rho(\mathbf{r}_p, \mathbf{r}, t)\,d\mathbf{r}. \quad (32)$$

Considering case I for evaluating the first derivative with respect to $\tilde{z}_p$ and $\tilde{\rho}_p$ as well as the form of V_{eff} given by Eq. (19), Eq. (30) can be simplified into two equations, viz.,

$$\begin{aligned} M_P \frac{d^2\tilde{\rho}_P}{dt^2} = &-\frac{Z_P Z_T \tilde{\rho}_P}{\left(\tilde{z}_P^2 + \tilde{\rho}_P^2\right)^{3/2}} \\ &- Z_P \int\left[\int \rho(\tilde{\rho}, \tilde{z}, t) J_0(k\tilde{\rho}) J_1(k\tilde{\rho}_P)\right. \\ &\left.\times e^{-k|\tilde{z}-\tilde{z}_P|}\,dk\right] d\mathbf{r} \end{aligned} \quad (33)$$

and

$$\begin{aligned} M_P \frac{d^2\tilde{z}_P}{dt^2} = &-\frac{Z_P Z_T \tilde{z}_P}{\left(\tilde{z}_P^2 + \tilde{\rho}_P^2\right)^{3/2}} \\ &+ Z_P \int\left[\int \rho(\tilde{\rho}, \tilde{z}, t) J_0(k\tilde{\rho}) J_0(k\tilde{\rho}_P)\right. \\ &\left.\times e^{-k|\tilde{z}-\tilde{z}_P|}\{\pm k\,dk\}\right] d\mathbf{r}. \end{aligned} \quad (34)$$

In Eq. (34), the ''$-$'' sign is taken if $\tilde{z} - \tilde{z}_P > 0$ and the ''$+$'' sign is taken if $\tilde{z} - \tilde{z}_P < 0$. In Eqs. (33) and (34), J_0 and J_1 are the zeroth-order and first-order Bessel functions, respectively.

The finite-difference (central) forms of Eqs. (33) and (34) can be written as

$$\tilde{\rho}_P^{n+1} = 2\tilde{\rho}_P^{n} - \tilde{\rho}_P^{n-1} + \frac{F_{\tilde{\rho}_P}^{n}(dt)^2}{M_P} \tag{35}$$

and

$$\tilde{z}_P^{n+1} = 2\tilde{z}_P^{n} - \tilde{z}_P^{n-1} + \frac{F_{\tilde{z}_P}^{n}(dt)^2}{M_P}, \tag{36}$$

where the index n defines the discretized time domain. $F_{\tilde{\rho}_P}^{n}$ on the right-hand side of Eq. (35) is given by

$$F_{\tilde{\rho}_P}^{n} = -\frac{Z_P Z_T \tilde{\rho}_P^{n}}{\left\{(\tilde{z}_P^{n})^2 + (\tilde{\rho}_P^{n})^2\right\}^{3/2}} - Z_P \int\left[\int \rho(\tilde{\rho}, \tilde{z}, t) J_0(k\tilde{\rho}) k J_1(k\tilde{\rho}_P^{n}) \times e^{-k|\tilde{z}-\tilde{z}_P^{n}|}\, dk\right] 2\pi\tilde{\rho}\, d\tilde{\rho}\, d\tilde{z}, \tag{37}$$

while $F_{\tilde{z}_P}^{n}$ on the right-hand side of Eq. (36) is given by

$$F_{\tilde{z}_P}^{n} = -\frac{Z_P Z_T \tilde{z}_P^{n}}{\left\{(\tilde{z}_P^{n})^2 + (\tilde{\rho}_P^{n})^2\right\}^{3/2}} - Z_P \int\left[\int \rho(\tilde{\rho}, \tilde{z}, t) J_0(k\tilde{\rho}) k J_1(k\tilde{\rho}_P^{n}) \times e^{-k|\tilde{z}-\tilde{z}_P^{n}|}\{\pm k\, dk\}\right] 2\pi\tilde{\rho}\, d\tilde{\rho}\, d\tilde{z}. \tag{38}$$

Equations (35) and (36) indicate that in order to obtain the projectile's position $(\tilde{\rho}_P^{n+1}, \tilde{z}_P^{n+1})$ at any advanced $(n+1)$-th time step from the nth time step, one needs the following quantities: (i) the electron density $\rho(\tilde{\rho}, \tilde{z}, \tilde{\rho}_p^{n}, \tilde{z}_p^{n}, t)$, (ii) the projectile's position at the nth time step $(\tilde{\rho}_p^{n}, \tilde{z}_p^{n})$, and (iii) the projectile's position at the $(n-1)$-th time step $(\tilde{\rho}_P^{n-1}, \tilde{z}_P^{n-1})$.

The electron density of the colliding system for any position $(\tilde{\rho}_P^{n}, \tilde{z}_P^{n})$ of the projectile can be calculated by solving Eq. (18). At any time, the second and third quantities above can be obtained from the knowledge of the same at the first and second time steps. The projectile's position at the first time step $(t = 0)$ is taken as

$$\tilde{z}_P^{(1)} = -\tilde{z}_P^{0};\ \tilde{\rho}_P^{(1)} = b, \tag{39}$$

while that at the second time step $(t = \Delta t)$ is taken as

$$\tilde{z}_P^{(2)} = -\tilde{z}_P^{(1)} + v_P \cos\vartheta_0\, \Delta t$$
$$\tilde{\rho}_P^{(2)} = \tilde{\rho}_P^{(1)} + v_P \sin\vartheta_0\, \Delta t. \tag{40}$$

Here, v_P is the projectile's incident velocity,

$$v_P = \left(\frac{2E_P}{M_P}\right)^{1/2}. \tag{41}$$

Thus, over a range of time, the realistic path of the projectile at any incident energy can be calculated. The integrals appearing in Eqs. (37) and (38) have been calculated by the trapezoidal method for the $\tilde{\rho}'$ and $\tilde{z}'$ variables, while a three-point Gauss quadrature has been employed for the variable k.

THE SOLUTION OF EQ. (18)

Following the discretization of the cylindrical space as described in the beginning of this section and with the position of the projectile, $\tilde{\rho}_P(t)$ and $\tilde{z}_P(t)$ as described in the above subsection, one solves the GNLSE [Eq. (18)] over a number of steps to obtain the two-centered hydrodynamical ''wave function''

$$\Psi(\tilde{\rho}, \tilde{z}, \tilde{\rho}_P, \tilde{z}_P, \Delta t),\ \Psi(\tilde{\rho}, \tilde{z}, \tilde{\rho}_P, \tilde{z}_P, 2\Delta t), \ldots,$$
$$\Psi(\tilde{\rho}, \tilde{z}, \tilde{\rho}_P, \tilde{z}_P, N_3\Delta t).$$

The parameters needed to launch the computations are included in Eqs. (18)–(41) and listed in Table I. The initial hydrodynamical density $\rho(\mathbf{r}, \mathbf{r}_P, 0)$ was calculated when $\mathbf{r}_P$ is infinitely large so that the entire density is concentrated in the target atom. The evaluation of $\rho(\mathbf{r}, \mathbf{r}_P, 0)$ is done by following an imaginary-time evolution of the hydrodynamical Eq. [60].

The calculated hydrodynamical ''wave function'' gives rise to various TD density-based properties. Details of the numerical scheme are reported elsewhere [48–50]. All computations were performed in double precision on a workstation.

DIFFERENT TIME-DEPENDENT PROPERTIES

Electronic Charge

The total electronic charge $N(t)$ within the entire grid as well as the charge $N_w(t)$ within a small window (w) of size $1.0 \times 10^{-12} \le \tilde{\rho} \le 2.92$, $-0.78 \le \tilde{z} \le 0.78$ that resides inside the full grid are

TABLE I
Parameters appearing in Eqs. (18) – (41); atomic units employed unless otherwise mentioned.

Parameters	Values
$\tilde{z}_P^0$	-18.0
ϑ_0	0°
Z_P	1.0(H^+), 6.0(C^{6+})
Z_T	2.0
Total mesh along $\tilde{\rho}$, N_1	100
Total mesh along $\tilde{z}$, N_2	257
Step-size, h	0.03
Step-size in time, Δt	0.08
x_0 [Eq. (28)]	1.0×10^{-6}
Lowest value for $\tilde{\rho}$	1.0×10^{-12}
Highest value for $\tilde{\rho}$	8.82090594
Lowest value for $\tilde{z}$	-3.84
Highest value for $\tilde{z}$	3.84
Total mesh for time, N_3	6160
M_P	1836.0(H^+), 11,016(C^{6+})

calculated as

$$N(t) = \int \rho(\tilde{\rho}, \tilde{z}, t)\tilde{\rho}\, d\tilde{\rho}\, d\tilde{z}\, d\tilde{\phi} \tag{42}$$

$$N_w(t) = \int_w \rho(\tilde{\rho}, \tilde{z}, t)\tilde{\rho}\, d\tilde{\rho}\, d\tilde{z}\, d\tilde{\phi}. \tag{43}$$

The value of $N(t)$ at any time indicates directly whether ionization is taking place or not, whereas $N_w(t)$ depicts the movement of electron density gliding in and out of the window.

Average Distances

The expectation values $\langle \tilde{\rho} \rangle(t)$ and $\langle r \rangle(t)$ are given by

$$\langle \tilde{\rho} \rangle(t) = \int \rho(\tilde{\rho}, \tilde{z}, t)\tilde{\rho}^2\, d\tilde{\rho}\, d\tilde{z}\, d\tilde{\phi} \tag{44}$$

$$\langle r \rangle(t) = \int \rho(\tilde{\rho}, \tilde{z}, t) r \tilde{\rho}\, d\tilde{\rho}\, d\tilde{z}\, d\tilde{\phi}, \tag{45}$$

where

$$r = (\tilde{\rho}^2 + \tilde{z}^2)^{1/2}. \tag{46}$$

These two parameters indicate how electron density spreads in the two-center potential as the interaction progresses.

Autocorrelation Function and Energy Spectrum

The complex autocorrelation function $C(t)$ with respect to the initial ($t = 0$) state is given by

$$C(t) = \int \Psi^*(\tilde{\rho}, \tilde{z}, 0)\Psi(\tilde{\rho}, \tilde{z}, t)\tilde{\rho}\, d\tilde{\rho}\, d\tilde{z}\, d\tilde{\phi}. \tag{47}$$

The survival probability of the initial ($t = 0$) state $P_{gs}(t)$ is

$$P_{gs}(t) = |C(t)|^2. \tag{48}$$

Obviously, the survival probability of the initial state depends on the energy spectrum.

The energy spectrum is calculated by a fast Fourier transform (FFT) of the time variable of the complex autocorrelation function [Eq. (47)], viz.,

$$\mathrm{ESD}(\omega) = \left| \int e^{-i\omega t} \langle \Psi(0) | \Psi(t) \rangle W(t)\, dt \right|^2, \tag{49}$$

where $W(t)$, the window function used to narrow down the integration limit from $(0, \infty)$ to $(0, T)$, is taken as

$$W(t) = 1 - \cos(2\pi t/T), \tag{50}$$

with $T = 327.6$ au, which corresponds to 2^{12} time steps.

Dipole Moment and External $\tilde{z}$ -Directional Field

The most important TD property for understanding the effect of the field due to the approaching projectile on the movement of electronic charge is the $\tilde{z}$-directional dipole moment of the electron, $\mu^{\tilde{z}}(t)$, which has been calculated as

$$\mu^{\tilde{z}}(t) = \int \rho(\tilde{\rho}, \tilde{z}, t)\tilde{z}\tilde{\rho}\, d\tilde{\rho}\, d\tilde{z}\, d\tilde{\phi}. \tag{51}$$

The perturbing $\tilde{z}$-directional field due to the projectile, which causes electron density to partially move away from the target nucleus, was calculated as follows:

$$\langle F_{\tilde{z}} \rangle(t) = \int \rho(\tilde{\rho}, \tilde{z}, t) F_{\tilde{z}}\, dV, \tag{52}$$

where

$$\begin{aligned} F_{\tilde{z}} &= -\nabla_{\tilde{z}} \left(-\frac{Z_P Z_T}{|\mathbf{r} - \mathbf{r}_P|} \right) \\ &= \frac{\partial}{\partial \tilde{z}} \left(\frac{Z_P Z_T}{|\mathbf{r} - \mathbf{r}_P|} \right). \end{aligned} \tag{53}$$

In other words,

$$F_{\tilde{z}} = \begin{cases} -Z_P Z_T \int J_0(k\tilde{\rho}) J_0(k\tilde{\rho}_P) e^{-k|\tilde{z}-\tilde{z}_P|} dk, \\ \qquad\qquad \text{if } \tilde{z} - \tilde{z}_P > 0 \\ Z_P Z_T \int J_0(k\tilde{\rho}) J_0(k\tilde{\rho}_P) e^{-k|\tilde{z}-\tilde{z}_P|} dk, \\ \qquad\qquad \text{if } \tilde{z} - \tilde{z}_P < 0. \end{cases} \quad (54)$$

Coulomb Energy

To understand the role of the projectile nucleus and correlation between the two electrons, one needs to calculate the Coulomb attraction energy due to the target nucleus and the interelectronic repulsion energy as follows:

$$E_{nu-el}(t) = -\int \frac{Z_T}{r} \rho(\tilde{\rho}, \tilde{z}, t) \tilde{\rho}\, d\tilde{\rho}\, d\tilde{z}\, d\tilde{\phi} \quad (55)$$

$$E_{el-el}(t) = \int \rho(\tilde{\rho}, \tilde{z}, t) \rho(\tilde{\rho}', \tilde{z}', t) J_0(k\tilde{\rho}) e^{-k|\tilde{z}-\tilde{z}'|} \times J_0(k\tilde{\rho}') \tilde{\rho}\tilde{\rho}'\, dk d\tilde{\rho}\, d\tilde{\rho}'\, d\tilde{z} d\tilde{z}'\, d\tilde{\phi}\, d\tilde{\phi}'. \quad (56)$$

Here, the integration with respect to k was performed by the Gauss–Legendre quadrature, that with respect to $\tilde{\rho}'$ and $\tilde{z}'$ by the trapezoidal method, and that with respect to $\tilde{\rho}$ and $\tilde{z}$ by the Simpson method.

Single-ionization Cross Section and Total Inelastic Cross Section

Assuming that the electronic charge reaching the periphery of the cylindrical grid experiences no force from the target nucleus, we describe the former by a free wave packet as

$$\theta = e^{ik\tilde{z}}, \quad (57)$$

where $k = mv/\hbar$ is the electronic wave number and $v = (2E_{el}/m)^{1/2}$. Thus, if one of the two electrons of the target atom becomes completely free, one can describe the single-ionization state as

$$\Psi_{SI} = N\theta\Psi_{He^+}, \quad (58)$$

where N is the normalization constant and Ψ_{He^+} is the wave function for He^+ in its ground state. Under such considerations, we define the single ionization probability $P_1^{ion}(t)$ as

$$P_1^{ion}(t) = |\langle \Psi(t) | \Psi_{SI}(t) \rangle|^2, \quad (59)$$

which has been calculated with

$$v = \left(\frac{2|E_{gs} - E_{FIT}|}{m} \right)^{1/2} \quad (60)$$

and

$$\Psi_{He^+} = \frac{1}{\pi^{1/2}} Z^{3/2} e^{-Zr}, \quad (61)$$

where E_{gs} and FIT are the ground-state energy and first ionization threshold, respectively, of the He atom.

The first ionization cross-section σ_1^{ion} is calculated as

$$\sigma_1^{ion}(b, E_P) = \left| b \frac{1}{T} \int P_1^{ion}(b, E)\, dt \right|^2, \quad (62)$$

while the total elastic and inelastic cross sections $\sigma^{el}(b, E)$ and $\sigma^{inel}(b, E)$, respectively, are given by

$$\sigma^{el}(b, E) = \left| b \frac{1}{T} \int P_{gs}(t)\, dt \right|^2 \quad (63)$$

and

$$\sigma^{inel}(b, E) = \left| b \frac{1}{T} \int [1 - P_{gs}(t)]\, dt \right|^2, \quad (64)$$

with $P_{gs}(t)$ given by Eq. (48).

TD Difference Density

The topographical change of electronic distribution in the cylindrical space due to the two-centered potential can be vividly described by the TD difference density,

$$\Delta\rho(\tilde{\rho}, \tilde{z}, t) = \rho(\tilde{\rho}, \tilde{z}, t) - \rho(\tilde{\rho}, \tilde{z}, 0). \quad (65)$$

Results and Discussion

The mechanism of A^{q+}–He collisions is studied through the time-evolution of the initial electron density $\rho(\mathbf{r}, t)$ which describes the collective dynamical behavior of all the electrons. The calcu-

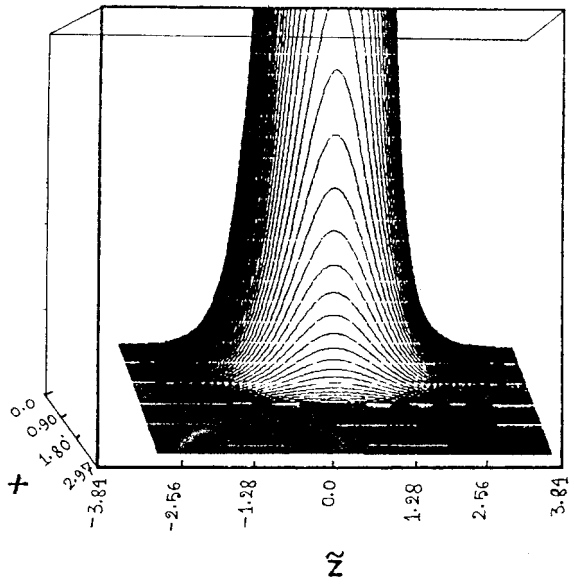

FIGURE 1. Perspective plots (au) of the initial (t = 0) hydrodynamical density $\rho(\tilde{\rho}, \tilde{z}, 0)$ corresponding to the $x\tilde{z}(x^2 = \tilde{\rho})$ plane.

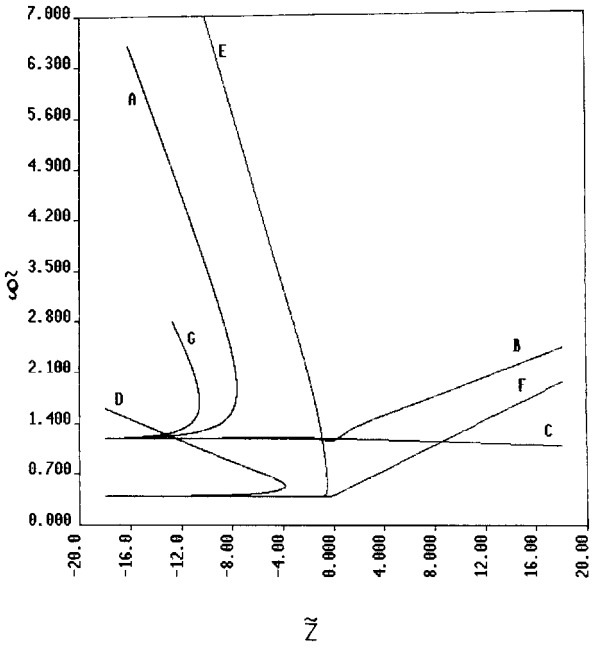

FIGURE 2. Trajectory of the projectiles in the $(\tilde{\rho}, \tilde{z})$ space. (A) corresponds to the projectile H^+ with $E = 100$ eV, $b = 1.2$ au; (B) to the projectile H^+ with $E = 1000$ eV, $b = 1.2$ au; (C), to the projectile H^+ with $E = 10{,}000$ eV, $b = 1.2$ au; (D), to the projectile H^+ with $E = 100$ eV, $b = 0.4$ au; (E), to the projectile H^+ with $E = 1000$ eV, $b = 0.4$ au; (F), to the projectile H^+ with $E = 10{,}000$ eV, $b = 0.4$ au; and (G), to the projectile C^{6+} with $E = 100$ eV, $b = 1.2$ au.

lated $\rho(\mathbf{r}, 0)$ (see the subsection on the solution of Eq. (27)), displayed in Figure 1, is cylindrically symmetric. The accuracy of this $\rho(\mathbf{r}, 0)$ is gauged by different quantities listed in Table II which shows a good agreement with HF values.

The projectile interacts with the He atom and affects the electron density which now comes under the force field of both the nuclei. The forward motion of the projectile continues until it is pushed back by the repulsive force of the target nucleus. Figure 2 shows the trajectories of the projectile obtained by solving the classical Hamilton's equation with the feedback of the electron density as described in the second section. The scattering of the projectile (Fig. 2) differs from that of Rutherford scattering in the sense that here the projectile's motion is governed by both the nuclear–nuclear repulsive (central field) as well as the nuclear–electron attractive forces. However, considering the motion of the projectile only under the influence of a central field, the nuclear–nuclear repulsive force, one obtains the Rutherford scattering angle $\Theta = \tan^{-1}[(Z_T Z_P)/(2E_P b)]$ for different trajectories as $\Theta(A) = 25.55°$, $\Theta(B) = 2.59°$, $\Theta(C) = 0.2598°$, $\Theta(D) = 68.45°$, $\Theta(E) = 7.78°$, $\Theta(F) = 0.779°$, and $\Theta(G) = 107.37°$, where the alphabets indicate different trajectories specified in Figure 2. Comparing the trajectories in Figure 2, we notice a deviation of the present scattering from Rutherford scattering. The deviation is greater for a smaller impact parameter (b) and a smaller projectile energy (E_p). For a high-projectile energy and high-impact parameter (e.g., $b = 1.2$ and $E = 10$ keV, trajectory C in Fig. 2), we see that the path of the projectile is almost the same as that of Rutherford. Again, for the projectile of larger mass (e.g., C^{6+}, $b = 1.2$, $E = 100$ eV, trajectory G in Fig. 2), the path is also nearly the same as that of Rutherford. Figure 2 shows that (i) the projectile moves

TABLE II

Comparison between the initial hydrodynamical wave function (HDWF) and the Hartree–Fock wave function (HFWF) for He in terms of different quantities (au.); the overlap integral between the two functions is 0.9943.

Quantities	HDWF	HFWF
$\langle r \rangle$	1.8539	1.8544
$\langle 1/r_{12} \rangle$	2.1013	2.0520
$\langle -Z/r \rangle$	−6.7497	−6.7492
$\langle \tilde{z} \rangle$	0.0	0.0

faster along the axis than along the radius of the cylinder, (ii) the projectiles C^{6+} ($E = 100$ eV, $b = 1.2$) and H^+ ($E = 100$ eV, $b = 1.2$) could not penetrate into the field of the target nucleus, whereas other projectiles could. Note that if the recoil energy of the projectile $E_P(t)$ at any time t is (i) greater than

$$-\int \frac{\rho(\mathbf{r})}{|\mathbf{r} - \mathbf{r}_\rho|}\, d\mathbf{r} + \frac{Z_P Z_T}{r_P},$$

then the projectile will proceed forward; (ii) equal to

$$-\int \frac{\rho(\mathbf{r})}{|\mathbf{r} - \mathbf{r}_P|}\, d\mathbf{r} + \frac{Z_p Z_T}{r_p},$$

then the projectile will come to a standstill at a distance r_p from the target nucleus and the formation of a pseudomolecule can be assumed; or (iii) less than

$$-\int \frac{\rho(\mathbf{r})}{|\mathbf{r} - \mathbf{r}_p|}\, d\mathbf{r} + \frac{Z_p Z_T}{r_p},$$

then after a certain time, the projectile will recede backward and there will be less energy transfer to the electron.

Although at any time the highest energy transferred to the electron is quite small, the total energy transferred to the electron from the projectile during the collision process from 0 to 492.8, 195.0, 57.25, 580.25, 202.0, 57.5, and 738.25 au for projectiles A, B, C, D, E, F, and G, respectively, in Figure 2 is substantial enough to cause the electron density to partly move away from the target nucleus and redistribute itself depending on the potential. The analysis provided in Appendix A would help explain the projectile–electron energy transfer. The fraction of energy transferred to the electron is 0.56 ($T = 256.48$), 0.21 ($T = 95.5$), 0.06 ($T = 28.5$), 0.63 ($T = 289.75$), 0.21 ($T = 96.75$), 0.06 ($T = 28.75$), and 0.18 ($T = 488.75$) for projectiles A, B, C, D, E, F, and G, respectively, in Figure 2. Thus, for a small impact parameter, the extent of energy transfer is higher, and for a fast projectile, it is lower. Furthermore, for a heavy projectile (C^{6+}), the energy transfer to the target electron is small. However, it is the total time of interaction which affects the extent of mixing of excited states of the He atom to the hydrodynamical ''wave function'' based on the symmetry of $\Psi(\mathbf{r}, 0)$. The displacement of electron density away from the target nucleus can occur due to the attraction of the projectile.

The excitation probability in slow collisions is very small [31] unless the two electronic states involved are nearly degenerate. This can be understood from an argument [61] according to which transitions are improbable unless

$$\frac{\Delta\varepsilon d_0}{\hbar v} \ll 1,$$

where $\Delta\varepsilon$ is the spacing between the energy levels; d_0, the range of interaction; and v, the relative velocity of the colliding species. Clearly, for small v ($\cong 100$ eV), the excitation probability will be quite small. Again, defining $\Delta t = d_0/v$ as the time of interaction of the colliding partners, the electronic energy is defined by the uncertainty principle only to within $\Delta\varepsilon \cong \hbar/\Delta t$. Thus, excitation to states having energies within this energy range of the initial state can only occur with high probability, but transitions to other states will be much less probable. Thus, for small v, although the time of interaction is high, $\Delta\varepsilon$ is small and, hence, higher excitation is hardly to occur; therefore, ionization is also unlikely.

Figure 3 shows $N(t)$ (label A), $N_w(t)$ (label C), and $P_{gs}(t)$ (label B) for H^+ with $E = 100$ eV and $b = 1.2$ au only. Plots for other projectiles show

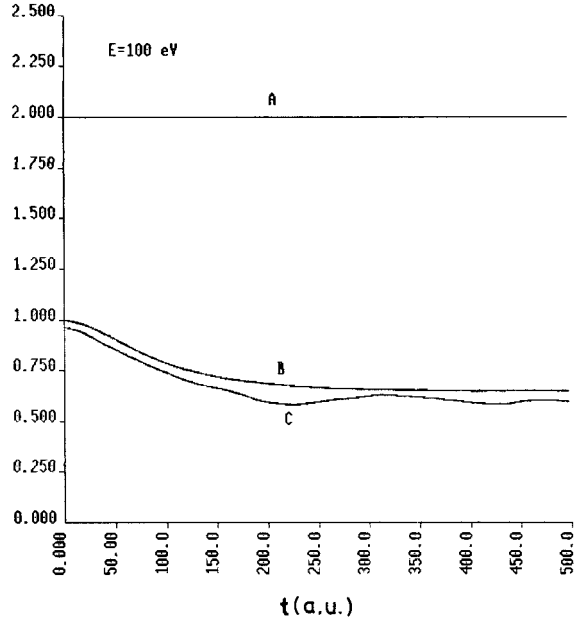

FIGURE 3. Plot of total number of electrons against time in au (A) within the full grid, $N(t)$, (C) within the window, $N_w(t)$, and (B) the survival probability of the initial ($t = 0$) state. This corresponds to the projectile H^+ with $E = 100$ eV and $b = 1.2$ au.

near-similar behavior. From these figures, we see that $N(t)$ remains fixed at 2, whereas a loss of density occurs from the vicinity of the He nucleus. For example, at $t = 214.72$ au, the window has lost 39.3% of its initial electronic charge (0.9602) when the projectile's position is $\tilde{z}_P = -8.0249$ and $\tilde{\rho}_P = 1.5681$. A monotonic fall in $N_w(t)$ is observed up to $t = 140.0$ au, after which its rate of change becomes quite small; for $t > 256.48$ au, $N_w(t)$ becomes nearly constant. This implies that once the projectile has altered its direction of motion the target nucleus resumes control of the residual electron density. The loss of electron density from the nuclear site leads to an increase in the expectation values of $\tilde{\rho}$ and r (refers to the target nucleus).

A smooth monotonic increase in both $\langle r \rangle$ and $\langle \tilde{\rho} \rangle$ is observed in Figure 4 (A) and (B), respectively, up to $t = 295.04$ au. For $t > 295.04$ au the values change with time to a lesser extent. The highest value of $\langle \tilde{\rho} \rangle$ is found to be 4.6734 at $t = 386.4$ au when $\tilde{z}_P = -10.739$ and $\tilde{\rho}_P = 3.9079$, whereas the highest value for $\langle r \rangle$ is 5.0017 au at $t = 386.32$ au when $\tilde{z}_P = -10.7324$ and $\tilde{\rho}_P = 3.9061$. However, at the time of the closest approach of the projectile, $t = 256.48$ au, $\langle \tilde{\rho} \rangle = 4.2119$, and $\langle r \rangle = 4.6393$. Again, the plots of $\langle r \rangle$ and $\langle \tilde{\rho} \rangle$ are given for the projectile H^+ with $E = 100$ eV and $b = 1.2$ au. The increase in the average electronic distance (Fig. 4) measured from the target nucleus is due to the change in the Coulomb attraction energy $\langle -Z/r \rangle$ of the electron with respect to the residual target nucleus and the interelectronic Coulomb repulsion energy, $\langle 1/r_{12} \rangle$, shown in Figure 4 (D) and (C), respectively. An increase in the $\langle -Z/r \rangle$ and a decrease in $\langle 1/r_{12} \rangle$ occur as the projectile approaches closer to the target. However, once the projectile's direction of motion is altered, both the values change very little. In other words, as already mentioned, the target nucleus reasserts control over the electronic density that is left to itself. Note, however, that as the proton recedes, the electron density does not return to its original state. The projectile-to-electron momentum transfer leading to the electron density moving away from the target nucleus will be facilitated if the nucleus has greater electron density around itself. Thus, Figure 4 shows that with the passage of time the rate of electrons moving away from the target nucleus decreases because of the lesser density around the nucleus, whereas, initially, the spread of density away from the target nucleus was larger. This leads to an initial, faster fall of both $\langle -Z/r \rangle$ and $\langle 1/r_{12} \rangle$ which become near-asymptotic as the projectile alters its direction. The values of $\langle -Z/r \rangle$ and $\langle 1/r_{12} \rangle$ at $t = 256.48$ au are -3.809 and 0.5242, respectively. Note that the total Coulombic attraction for the electron density is given by

$$E = -\int \frac{Z_P \rho(\mathbf{r}, t)}{|\mathbf{r} - \mathbf{r}_P|} d\mathbf{r} - \int \frac{Z_T \rho(\mathbf{r}, t)}{r} d\mathbf{r}.$$

Figure 4 shows the attraction due to the target only; the total Coulombic attraction will be more negative than the value shown in Figure 4.

The phenomenon of collision at low-projectile energy can be regarded as a competition between the target (by its attraction energy $\langle -Z/r \rangle$) and the projectile (by its attraction energy $\langle -Z_p/|\mathbf{r} - \mathbf{r}_P| \rangle$) for the electrons. Since the electrons were initially in the target, and the nuclear charge of the target is twice that of the projectile (H^+), most of the electron density remains under the control of the target. However, by transferring some of its momentum to the target-controlled electron density, the projectile can cause a part of the density to move away from the target nucleus and by attraction drag the density on to its direction of approach. However, since the momentum trans-

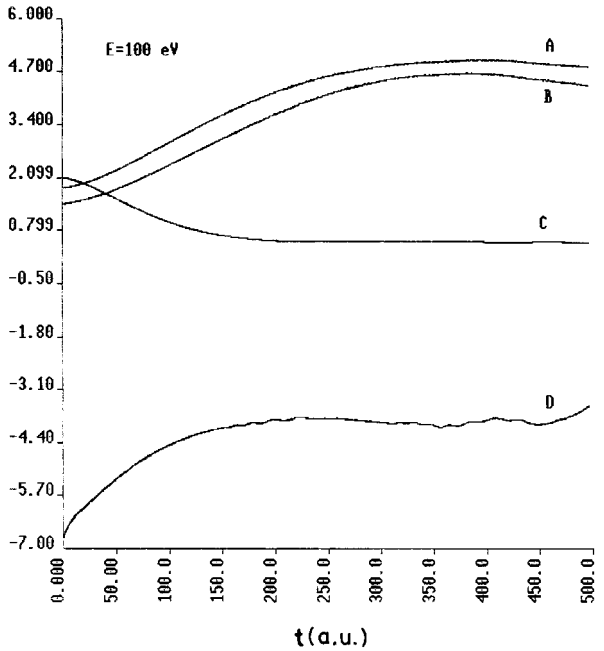

FIGURE 4. Time-dependent (A) $\langle r \rangle(t)$, (B) $\langle \tilde{\rho} \rangle(t)$, (C) $\langle 1/r_{12} \rangle(t)$, and (D) $-\langle Z_T/r \rangle(t)$ plotted against time, in au. The projectile is H^+ with $E = 100$ eV and $b = 1.2$ au.

ferred to the electron cannot be taken away, electron density does not go back to its original state even when the projectile has effectively left (see below for density plots).

Figure 3 (B) depicts the survival probability $P_{gs}(t)$ of the initial target state which helps to keep track of the extent of electron loss by the target nucleus and consequent excitation by the projectile H^+ with $E = 100$ eV and $b = 1.2$ au. A near-asymptotic value of $P_{gs}(t)$ is reached once the projectile alters its direction. Being a cosine function [Eq. (48)], the survival probability decreases monotonically from its initial ($t = 0$) value of unity, and at $t = 256.48$ au, P_{gs} falls to 0.6634. Thus, electronic excitation occurs as a result of projectile–electron momentum transfer.

Figures 5 and 6 display the TD $\tilde{z}$-directional external average field and dipole moment $\mu^{\tilde{z}}(t)$, respectively, for a number of projectiles. A correspondence between these two quantities can be seen from Figures 5 and 6 in the sense that (i) both are small-valued and (ii) the negative (positive) external field gives rise to a negative (positive) dipole moment. Figure 5 clearly shows that during its approach the projectile drags electron density toward itself. However, a time lag in the response of the electron density to the projectile is noticed in all the cases, e.g., for H^+, with $E = 100$ eV and $b = 1.2$ au, the minimum in the average field [Fig. 5 (A)] occurs at $t = 236.5$ au, whereas that in the dipole moment [Fig. 6 (A)] occurs at $t = 317.6$ au.

Figure 7 displays the energy spectral density ESD(ω) corresponding to $\rho(\mathbf{r}, t)$ at $t = 327.6$ au for the projectile H^+ with $E = 100$ eV and $b = 1.2$. ESD(ω) arises from different elementary states corresponding to the hydrodynamical density at this instant. The logarithmic energy spectrum (Fig. 7) gives the distribution of eigenstates over an energy domain $-42.15 \leq E \leq 36.37$. The largest

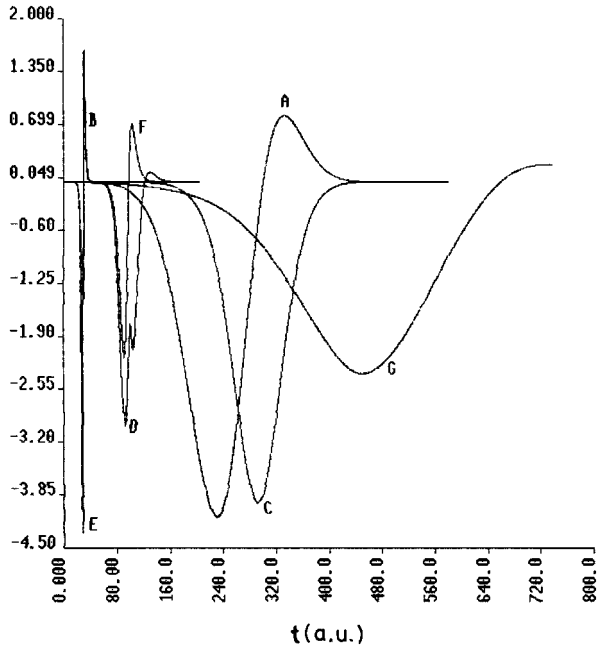

FIGURE 5. Time-dependent average $\tilde{z}$-directional external perturbative field, $\langle F_{\tilde{z}} \rangle(t) \times f$, for different projectiles plotted against time, in au, where f = 10,000, 1, 50, 2, 2, 2, and 10,000 for (A), (B), (C), (D), (E), (F), and (G), respectively. (A) corresponds to projectile H^+ with $E = 100$ eV, $b = 1.2$ au; (B), to projectile H^+ with $E = 10$ keV, $b = 1.2$; (C), to projectile H^+ $E = 100$ eV, $b = 0.4$ au; (D), to projectile H^+ with $E = 1$ keV, $b = 0.4$ au; (E), to projectile H^+ with $E = 10$ keV, $b = 0.4$ au; (F), to projectile H^+ with $E = 1$ keV, $b = 1.2$ au; and (G), to projectile C^{6+} with $E = 100$ eV, $b = 1.2$ au.

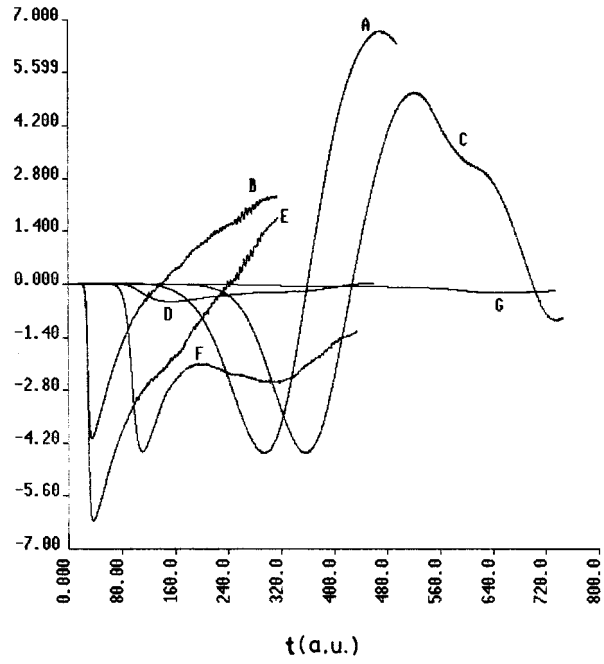

FIGURE 6. Time-dependent, $\tilde{z}$-directional dipole moment of the electronic charge distribution, $\mu^{\tilde{z}}(t) \times f$, for different projectiles plotted against time, in au, where f = 10,000, 1000, 100, 2, 1000, 100, and 1000 for (A), (B), (C), (D), (E), (F), and (G), respectively. (A) corresponds to projectile H^+ with $E = 100$ eV, $b = 1.2$ au; (B), to projectile H^+ with $E = 10$ keV, $b = 1.2$; (C), to projectile H^+ with $E = 100$ eV, $b = 0.4$ au; (D), to projectile H^+ with $E = 1$ keV, $b = 0.4$ au; (E), to projectile H^+ with $E = 10$ keV, $b = 0.4$ au; (F), to projectile H^+ with $E = 1$ keV, $b = 1.2$ au; and (G), to projectile C^{6+} with $E = 100$ eV, $b = 1.2$ au.

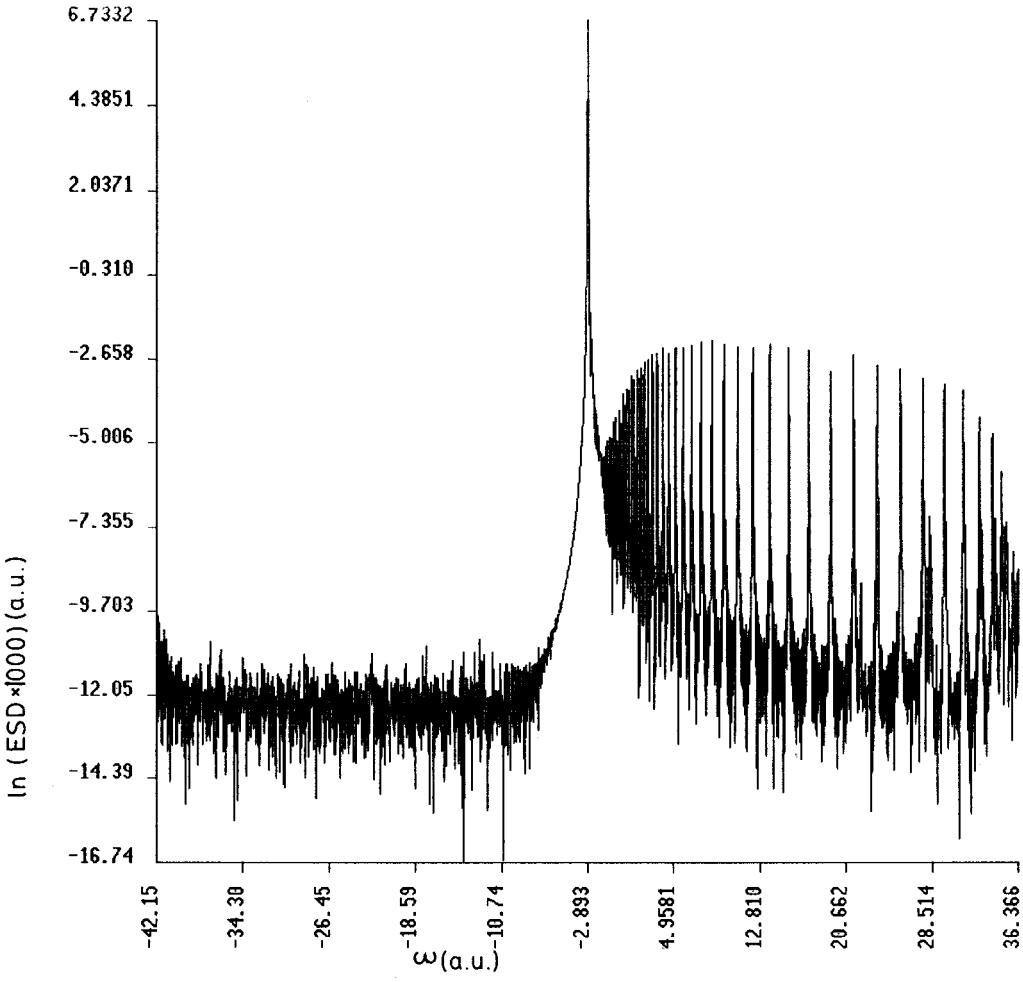

FIGURE 7. The logarithm of the energy spectral density, ln(ESD $\times$ 1000), plotted against ω, in au. A continuum band of very low ESD was calculated. This corresponds to the projectile H^+ with E = 100 eV and b = 1.2 au.

contributions to the spectrum arise from the bound states (negative energy) of the He atom which lie close to the ground state. The continuum (positive energy) band appearing on the right-hand side of the main peak has very little (ESD $\cong 10^{-6}$ au) contribution to the energy spectrum at $t = 327.6$ au. This fact can also be explained from the imaginary part of autocorrelation function. We have

$$C^{im} = -\sum_{m=\text{bound}} |\alpha_m|^2 \sin(E_m t) - \sum_{n=\text{continuum}} |\alpha_n|^2 \sin(E_n t) = A - B,$$

where A and B are the contributions from bound and continuum states, respectively. Obviously, the above expression can lead to an irregular behavior of C^{im} in the course of time. The ground state of the He atom ($E = -2.90349$ au) has the highest ESD (0.8398 au). Accordingly, the elastic cross section calculated has the value $\sigma^{el} = 2.087 \times 10^{-16}$ cm^2, whereas the value of the inelastic cross section, $\sigma^{inel} = 3.170 \times 10^{-18}$ cm^2.

The TD single-ionization probability (Fig. 8) indicates that although this is initially small its value increases when the projectile alters its direction. The highest value of the single-ionization probability is 0.1635 at $t = 386.56$ for H^+ with $E = 100$ eV, $b = 1.2$; 0.1799 at $t = 402.0$ for H^+ with $E = 100$ eV, $b = 0.4$; 0.138 at $t = 384.5$ for H^+ with $E = 1000$ eV, $b = 0.4$; 0.152 at $t = 384.5$ for H^+ with $E = 1000$ eV, $b = 1.2$; and 0.184 at $t = 401.75$ for C^{6+} with $E = 100$ eV, $b = 1.2$. Thus, very little or no ionization takes place. Table III shows the single-ionization cross sections (σ_1^{ion}) for different projectiles: (i) σ_1^{ion} decreases with increase in the

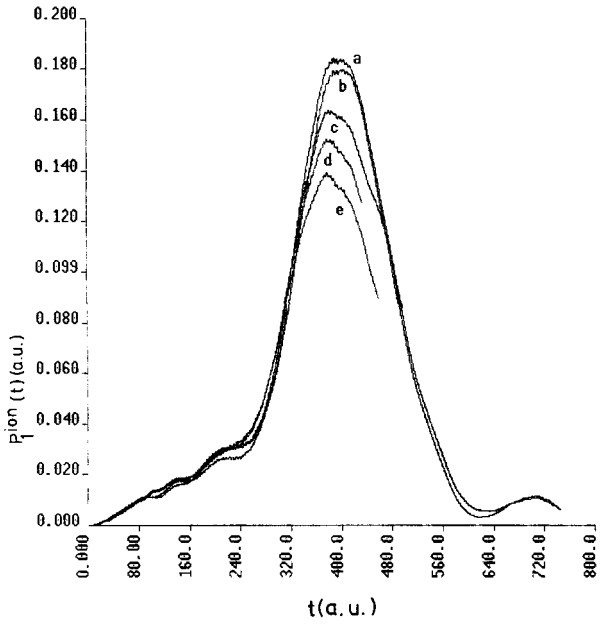

FIGURE 8. Time-dependent single-ionization probability, $P_1^{\text{ion}}(t)$, plotted against time, in au, for different projectiles, viz., (a) C^{6+} with $E = 100$ eV, $b = 1.2$ au; (b) H^+ with $E = 100$ eV, $b = 0.4$ au; (c) H^+ with $E = 100$ eV, $b = 1.2$ au; (d) H^+ with $E = 1$ keV, $b = 1.2$ au; and (e) H^+ with $E = 1$ keV, $b = 0.4$ au.

projectile energy because of the lesser time of interaction, (ii) σ_1^{ion} decreases with decrease in the impact parameter, and (iii) for C^{6+}, σ_1^{ion} is less than that for H^+ with the same b and E because C^{6+} remains farther away from the target atom.

The detailed features of electron density depend on the states mixed in the hydrodynamical ''wave function'' due to the TD interaction. Expressing the hydrodynamical ''wave function'' $\Psi(\mathbf{r}, t)$ in terms of different elementary states (ϕ_i), one can obtain a number of coupled equations for the mixing coefficients of the states. Based on the symmetry of the colliding system, it is possible to obtain information about those states which only would contribute to $\Psi(\mathbf{r}, t)$ and thus the number of coupled equations can be reduced. The electronic Hamiltonian in the present case is symmetric under reflection with respect to the Cartesian x and y axes, whereas it is antisymmetric in the z-axis. In other words, the electronic Hamiltonian appearing in Eq. (11) is such that it is biased along the $\tilde{z}$-axis (because the projectile is approaching from the left along $\tilde{z}$) and unbiased along the $\tilde{\rho} = (x^2 + y^2)^{1/2}$ axis. Note that the initial hydrodynamical state is symmetric in the $(\tilde{\rho}, \tilde{z})$-collision plane. Thus, at

TABLE III
Total single-ionization cross sections.

Projectile	E_p (eV)	b (au)	σ_1^{ion} (cm^2)
H^+	100	1.2	1.628×10^{-19}
H^+	1000	1.2	1.213×10^{-19}
H^+	10,000	1.2	2.136×10^{-20}
H^+	100	0.4	1.141×10^{-20}
H^+	1000	0.4	1.309×10^{-20}
H^+	10,000	0.4	2.320×10^{-21}
C^{6+}	100	1.2	1.145×10^{-19}

any time during the interaction, the hydrodynamical ''wave function'' will have contributions from those states which are (i) $\tilde{z}$-antisymmetric (''$-$'' sign below) and/or (ii) $\tilde{\rho}$-symmetric (''$+$'' sign below). Thus, we have the following selection rules in the present A^{q+}–He collision:

$$\Psi(\tilde{\rho}, \tilde{z}, 0) \rightarrow +(\tilde{\rho}\text{-direction})$$
$$\Psi(\tilde{\rho}, \tilde{z}, 0) \rightarrow -(\tilde{z}\text{-direction}).$$

In other words, states such as p_z, d_{z^2}, d_{xz}, and d_{yz} cannot contribute to Ψ, whereas p_x, p_y, $d_{x^2-y^2}$, d_{xy}, etc., can contribute. Thus, one expects that density would spread more along the $\tilde{\rho}$-direction than along the $\tilde{z}$-direction. This fact is clearly seen from the topographical change of the electron density in the $(\tilde{\rho}, \tilde{z})$ space for, e.g., H^+ with $E = 100$ eV and $b = 1.2$ au, shown in Figure 9. Density is accumulated more along the $\tilde{\rho}$-direction than along the $\tilde{z}$-direction while being depleted at the He nucleus.

The direction of the unit electronic current vector at different points in the $(\tilde{\rho}, \tilde{z})$-space can also be seen from Figure 10 for, e.g., H^+ with $E = 100$ eV and $b = 1.2$ au. The movement of electron density at different points in the $(\tilde{\rho}, \tilde{z})$ space is in the opposite direction to that of the current vector.

Conclusion

In terms of density-based quantities, the quantum fluid dynamical equation of motion provides an effective, alternative way of looking at TD processes such as ion–atom collisions. Because of the simplicity associated with the electron density, detailed insights into the *mechanism* of the collision process can be obtained, without great computational labor, by following the process from start to finish in real time. At any instant of time, the TD

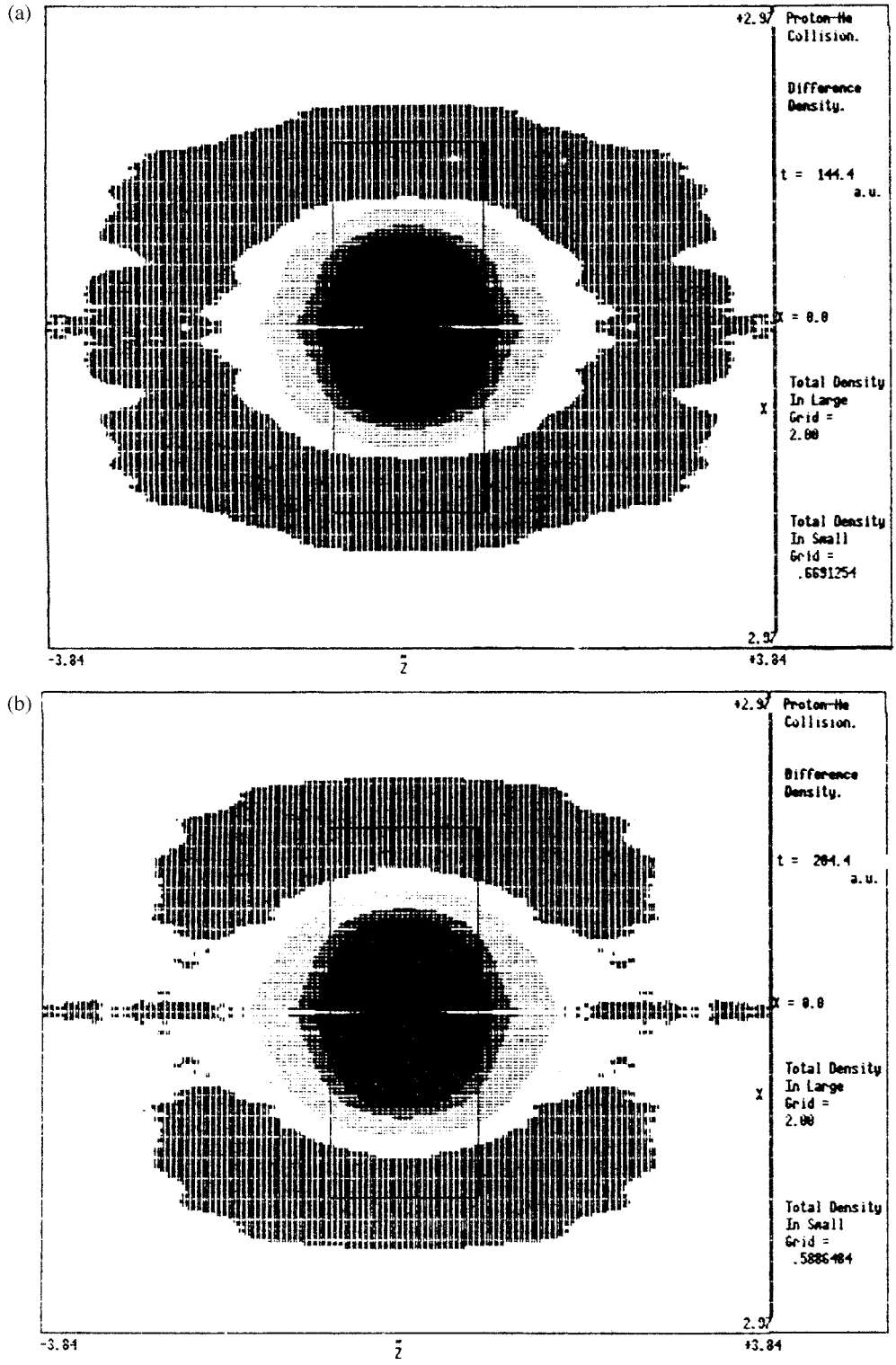

FIGURE 9. Projected difference density, $\Delta\rho(\tilde{\rho}, \tilde{z}, t)$, maps in the $(\tilde{\rho}, \tilde{z})$ plane, in au. Both the computation grid and the window are shown. The central dark region (He nucleus at its center) and the dotted halo surrounding it correspond to the decrease in electron density, while the other parts with straight lines correspond to the increase in the same. (a) $t = 144.4$ au; (b) $t = 204.4$ au; (c) $t = 264.4$ au; (d) $t = 354.4$ au. This corresponds to the projectile H^+ with $E = 100$ eV and $b = 1.2$ au.

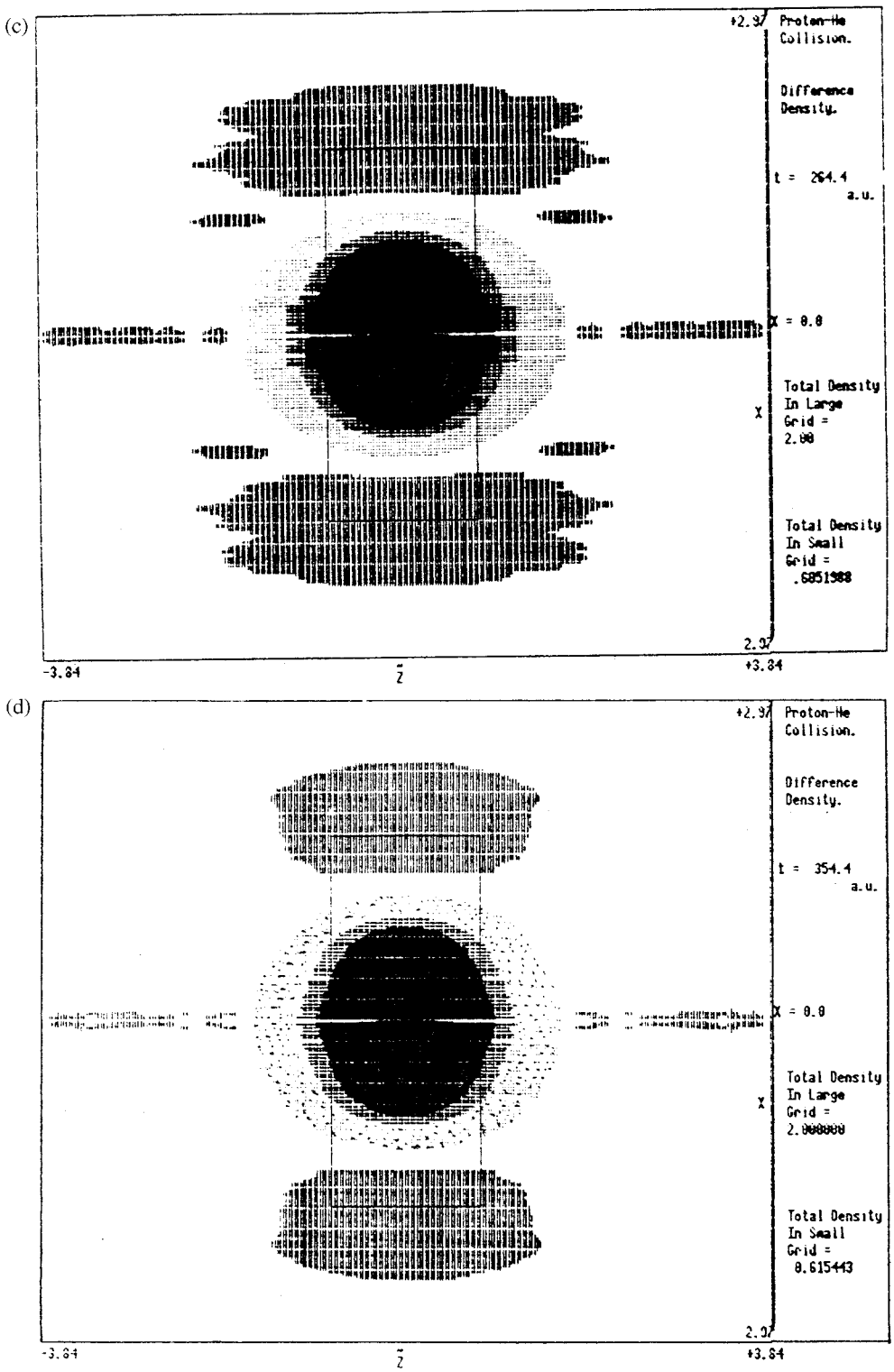

FIGURE 9. Continued.

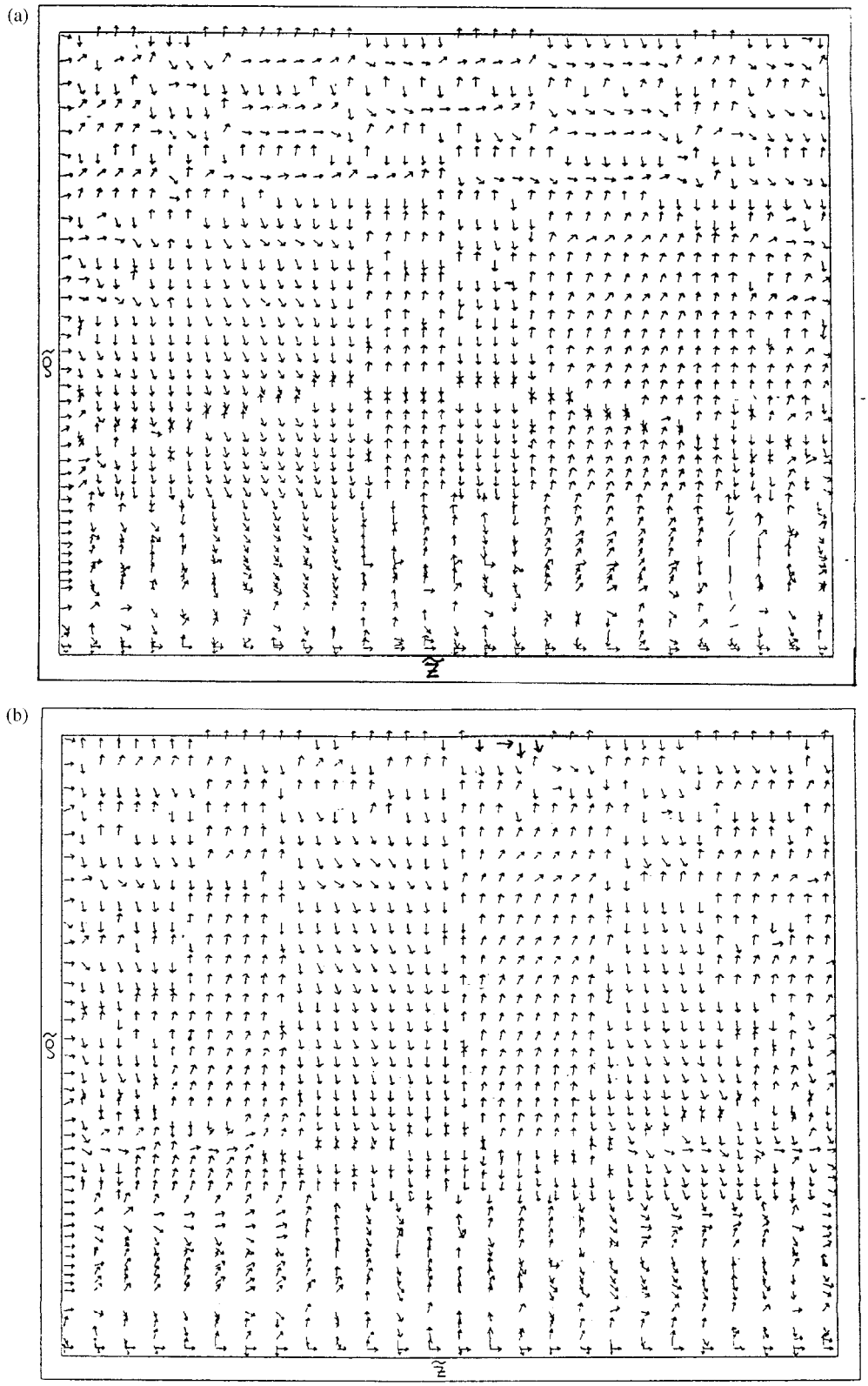

FIGURE 10. Unit current density vectors (au) at different points in the $x\tilde{z}(x^2 = \tilde{\rho})$ plane. (a) t = 144.4 au; (b) t = 204.4 au; (c) t = 264.4 au; (d) t = 354.4 au. This corresponds to the projectile H^+ with E = 100 eV and b = 1.2 au.

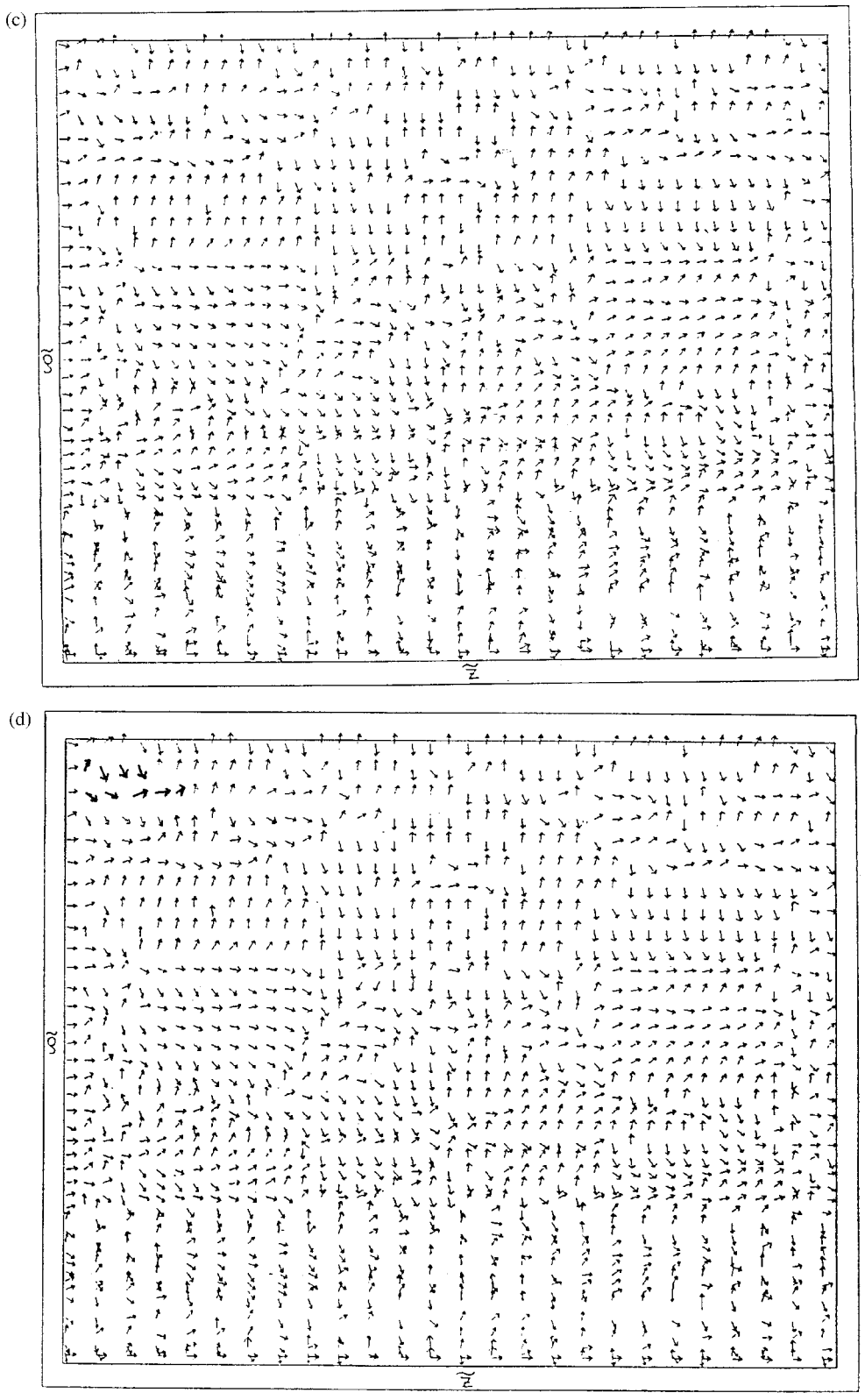

FIGURE 10. Continued.

electron density can be analyzed through, e.g., a fast Fourier transform to identify the various excited states which could mix with the initial state as a result of the interaction. In view of the difficulties associated with the solution of the TD Schrödinger equation for real systems, the results and their interpretations presented in this article demonstrate that one now has a general TD quantum mechanical equation of motion in three-dimensional space which not only deals with weak, strong, very strong, and extremely strong interaction with high accuracy, but also yields attractive and transparent physical insights. Following the present approach, trajectory calculations for atomic and molecular collisions may now be performed, subject to the TD electron density.

ACKNOWLEDGMENTS

We thank the Council of Scientific and Industrial Research, New Delhi, the Department of Atomic Energy, Bombay, and the Jawaharlal Nehru Centre for Advanced Scientific Research, Bangalore, for financial support. We also thank Prof. N. Sathyamurthy for his assistance.

Appendix A

Since no third body is present to drain away either the energy or the momentum, the total energy and momentum will be conserved at any time, i.e.,

$$\frac{M_P v_0^2}{2} = \frac{M_P v_P^2}{2} + \frac{m v_e^2}{2} \tag{A.1}$$

and

$$M_P v_0 = M_P v_P + m v_e, \tag{A.2}$$

where v_0, v_P, and v_e denote the incident speed of the projectile, the speed of the projectile, and the speed of electron at any time, respectively.

From Eqs. (A.1) and (A.2), we have

$$v_e = v_P + v_0, \text{ at any time.} \tag{A.3}$$

$$\text{Since } v_P \ll v_0,\ v_e \le 2v_0; \text{ hence, } v_e^{max} = 2v_0. \tag{A.4}$$

The total energy transferred to the electron at any time is given by

$$\frac{1}{2} m v_e^2 = \frac{1}{2} m (v_0 + v_P)^2. \tag{A.5}$$

The total energy transferred to the electron for the entire duration of collision (0 to T) is given by

$$\int_0^T \frac{1}{2} m (v_0 + v_P)^2 \, dt. \tag{A.6}$$

The highest energy transferred to the electron from 0 to T is

$$\frac{1}{2} m v_0^2 4 \int_0^T dt = 2 m v_0^2 T. \tag{A.7}$$

The fraction of energy transferred is

$$\frac{4 m v_0^2 T}{M_p v_0^2} = 4 \frac{m}{M_p} T. \tag{A.8}$$

References

1. S. Datz, R. Hippler, L. H. Andersen, P. F. Dittner, H. Knudsen, H. F. Krause, P. D. Miller, P. L. Pepniller, T. Rossel, R. Schuch, N. Stolterfoht, Y. Yanazaki, and C. R. Vane, Phys. Rev. A **41,** 3559 (1990).
2. J. E. Miraglia and V. D. Rodriguez, in *Proceedings of the* 17*th International Conference on Physics of Electronic and Atomic Collisions*, W. R. MacGilliray, I. E. McCarthy, and M. C. Standage, Eds. Adam Hilger, Bristol, 1992.
3. K. Runge, D. A. Micha, and E. Q. Feng, Int. J. Quantum Chem. **24,** 781 (1990).
4. E. Deumens, A. Diz, H. Taylor, and Y. Öhrn, J. Chem. Phys. **96,** 6820 (1992).
5. M. W. Gealy and B. V. Zyl, Phys. Rev. A **36,** 3091 (1987).
6. M. Kimura and C. D. Lin, Phys. Rev. A **34,** 176 (1986).
7. J. Burgdörfer and L. J. Dubé, Phys. Rev. Lett. **52,** 2225 (1984).
8. T. G. Winter, Phys. Rev. A **44,** 4353 (1992).
9. J. Macek and C. Wang, Phys. Rev. A **34,** 1787 (1986).
10. T. Ishihara and J. H. McGuire, Phys. Rev. A **38,** 3310 (1988).
11. K. C. Kulander, K. R. Sandhya Devi, and S. E. Koonin, Phys. Rev. A **25,** 2968 (1982).
12. N. Shimakura, H. Sato, M. Kimura, and T. Wanatabe, J. Phys. B **20,** 1801 (1987).
13. B. M. Deb, P. K. Chattaraj, and S. Mishra, Phys. Rev. A **43,** 1248 (1991).
14. R. Shingal and C. D. Lin, J. Phys. B **24,** 251 (1991).
15. W. Fritsch and C. D. Lin, J. Phys. B **19,** 2683 (1986).
16. H. Ast, H. J. Lüdde, and R. M. Dreizler, J. Phys. B **23,** 2305 (1990).
17. D. Dowek, C. J. Houver, J. Pommier, C. Richter, T. Royer, N. Andersen, and B. Palsdottier, Phys. Rev. Lett. **64,** 1713 (1990).

18. C. J. Houver, D. Dowek, C. Richter, and N. Andersen, Phys. Rev. Lett. **68,** 162 (1992).
19. C. Richter, N. Andersen, C. J. Brenot, D. Dowek, C. J. Houver, J. Salgado, and W. J. Thomson, J. Phys. B **26**, 723 (1993).
20. R. Hippler, O. Plotzke, W. Harbich, H. Madeheim, H. Kleinpoppen, and O. H. Lutz, Z. Phys. D **18,** 61 (1991).
21. R. A. Cline, W. B. Westerveld, and J. S. Risley, Phys. Rev. A **43,** 1611 (1991).
22. J. L. Shinpaugh, J. M. Sanders, J. M. Hall, D. H. Lee, H. Schmidt-Böcking, T. N. Tipping, T. J. M. Zouras, and P. Richard, Phys. Rev. A **45,** 2922 (1992).
23. M. E. Rudd, Y. K. Kim, D. H. Madison, and T. J. Gay, Rev. Mod. Phys. **64,** 441 (1992).
24. E. Deumens, A. Diz. R. Longo, and Y. Öhrn, Rev. Mod. Phys. **66,** 917 (1994).
25. Dz. Delkic, R. Gayet, and A. Salim, Phys. Rep. **56C,** 279 (1979).
26. L. Kocbach, J. M. Hansteen, and R. Gundersen, Nucl. Instrum. Methods **169,** 281 (1980).
27. K. Dettmann and G. Leibfriend, Z. Phys. **218,** 1 (1969).
28. U. Fano and W. Lichten, Phys. Rev. Lett. **14,** 627 (1965).
29. U. Wille and R. Hippler, Phys. Rep. **132,** 129 (1986).
30. A. Jain, C. D. Lin, and W. Fritsch, J. Phys. B **21,** 1545 (1988).
31. J. B. Delos, Rev. Mod. Phys. **53,** 287 (1981).
32. M. Kimura and N. F. Lane, in *Advances in Atomic, Molecular and Optical Physics*, D. Bates and B. Bederson, Eds. (Academic Press, New York, 1980).
33. A. Riera, in *Time-Dependent Quantum Molecular Dynamics*, J. Broeckhove and I. Lathouwers, Eds. (Plenum, New York, 1992).
34. D. H. Tiszauer and K. C. Kulander, Comput. Phys. Commun. **63,** 351 (1991).
35. D. A. Micha and K. Runge, in *Time-Dependent Quantum Molecular Dynamics*, J. Broeckhove and I. Lathouwers, Eds. (Plenum, New York, 1992).
36. B. M. Deb and P. K. Chattaraj, Phys Rev A **39,** 1696 (1989).
37. R. Car and M. Parrinello, Phys. Rev. Lett. **55,** 2471 (1985).
38. D. K. Remler and P. A. Madden, Mol. Phys. **70,** 921 (1990).
39. M. C. Payne, M. P. Teter, D. C. Allan, T. A. Arias, and J. D. Joannopoulos, Rev. Mod. Phys. **64,** 1045 (1992).
40. J. Theilhaber, Phys. Rev. B **46**, 12990 (1992).
41. N. Stolterfoht, D. Schneider, J. Tanis, H. Altevogt, A. Salin, P. D. Fainstein, R. Rivarola, J. P. Grandin, and J. N. Scheurer, Europhys. Lett. **4,** 899 (1987).
42. P. D. Fainstein, V. H. Ponce, and R. D. Rivarola, J. Phys. B **21,** 287 (1987).
43. R. G. Parr and W. Yang, *Density Functional Theory of Atoms and Molecules* (Oxford University Press, New York, 1989).
44. E. S. Kryachko and E. V. Ludeña, *Energy Density Functional Theory of Many-Electron Systems* (Kluwer, Dordrecht, 1990).
45. B. M. Deb and S. K. Ghosh, in *The Single-Particle Density in Physics and Chemistry*, N. H. March and B. M. Deb, Eds. (Academic Press, London, 1987).
46. B. M. Deb and S. K. Ghosh, J. Chem. Phys. **77,** 342 (1982).
47. C. Y. Wong, J. Math. Phys. **17,** 1008 (1976).
48. B. Kr. Dey and B. M. Deb, Int. J. Quantum Chem. **56,** 707 (1995).
49. B. Kr. Dey and B. M. Deb, Int. J. Quantum Chem., submitted.
50. B. Kr. Dey and B. M. Deb, Pramana-J. Phys. **48**, L849 (1997).
51. E. Runge and E. K. U. Gross, Phys. Rev. Lett. **52,** 997 (1984).
52. A. K. Dhara and S. K. Ghosh, Phys. Rev A **35,** 442 (1987).
53. M. Horbatsch and R. M. Dreizler, Z. Phys. A **300,** 119 (1981).
54. B. M. Deb, Ed., *The Force Concept in Chemistry* (Van Nostrand-Reinhold, New York, 1981).
55. H. J. C. Berendsen and J. Mavri, J. Phys. Chem. **97,** 13464 (1993).
56. A. Garcia-vela, R. B. Gerber, and D. G. Imre, J. Chem. Phys. **97,** 7242 (1992).
57. P. Bala, B. Lesyng, and J. A. McCammon, Chem. Phys. Lett. **219,** 259 (1994).
58. P. Bala, B. Lesyng, and J. A. McCammon, in *Quantum Mechanical Simulation Methods for Studying Biological Systems*, D. Bicout, M. Field, and A. Szabo, Eds. (Springer-Verlag, Heidelberg, 1996).
59. B. M. Deb and P. K. Chattaraj, Phys. Rev. A **45,** 1412 (1992).
60. B. Kr. Dey and B. M. Deb, to be published.
61. H. S. W. Massey, Rep. Prog. Phys. **12,** 248 (1949).